Additive Manufacturing 47 (2021) 102328

Contents lists available at ScienceDirect

Additive Manufacturing

journal homepage: www.elsevier.com/locate/addma

Research Paper

In situ infrared temperature sensing for real-time defect detection in additive manufacturing

Rifat-E-Nur Hossain [a], Jerald Lewis [a,b], Arden L. Moore [a,b,*]

[a] Institute for Micromanufacturing, Louisiana Tech University, Ruston, LA 71272, USA
[b] Mechanical Engineering Dept., Louisiana Tech University, Ruston, LA 71272, USA

ARTICLE INFO

Keywords:
In situ sensing
Process monitoring
Defect identification
Statistical analysis
Machine learning

ABSTRACT

Melt pool temperature is a critical parameter for the majority of additive manufacturing processes. Monitoring of the melt pool temperature can facilitate the real-time detection of various printing defects such as voids, over-extrusion, filament breakage, clogged nozzle, etc. that occur either naturally or as the result of malicious hacking activity. This study uses an in situ, multi-sensor approach for monitoring melt pool temperature in which non-contact infrared temperature sensors with customized field of view move along with the extruder of a fused deposition modeling-based printer and sense melt pool temperature from a very short working distance regardless of its X-Y translational movements. A statistical method for defect detection is developed and utilized to identify temperature deviations caused by intentionally implemented defects. Effective detection for multiple defect types and sizes is demonstrated using both a simple L-shaped test geometry and a more complex industry standard test article. Strengths and limitations of this approach are presented, and the potential for expansion via more advanced data analysis techniques such as machine learning are discussed.

1. Introduction

Fused deposition modeling (FDM) is one of the most promising and continuously growing additive manufacturing (AM) techniques that possesses the advantages of printing lightweight and complex parts with fewer operational steps [1,2]. Unlike conventional manufacturing, internal features are printed at the same time as the structure, which eliminates further processing steps and use of expensive tools [3]. Moreover, material deposition in specific print location ensures effective material consumption and low product final weight [2]. Along with these advantages, this manufacturing technology can present unique challenges in terms of mechanical performance and dimensional accuracy. Some major issues of FDM include pore/void formation, over-extrusion, shrinkage, corner warping, delamination, and clogging of material in the nozzle [4]. These defects can lead to high dimensional error and poor mechanical properties [5]. In certain cases, the number or severity of defects can require reprinting of the entire part which increases material usage and lead time. Besides naturally occurring defects, malicious entities may seek to induce defects as a means of sabotaging printed parts via hacking of the printing apparatus. Thus, it is advantageous to implement in situ condition monitoring whenever possible in order to take corrective measures during the print or abort the print entirely in the case of a critical defect condition. Also, when consistent quality assurance is a requirement, AM becomes unreliable without the aid of in situ quality monitoring measures [6]. In the longer term, in situ process monitoring with real-time defect detection will create new possibilities to establish a self-adaptive system with sophisticated machine learning-enabled prediction features, which will transform AM into a more dependable and commercially viable technique [1,7].

A crucial parameter for any AM process involving a thermoplastic polymer is the temperature of the melted region, which dictates viscosity within the melt and thermal residual stress build-up during solidification [8,9]. Because temperature affects the way in which the molten materials flows, accumulates, and bonds to the existing materials, the temperature of the extruded material has a strong influence on the formation of defects, inter-layer bonding strength, and other aspects of the print which are critical to its final performance [10]. Thus, deviations of temperature within the melted region can be a strong indicator of a printing defect. Physically, a lack of extruded material may lead to a void and correspond to a lower than expected temperature as the cooler material underneath remains exposed for example, while an

* Corresponding author at: Institute for Micromanufacturing, Louisiana Tech University, Ruston, LA 71272, USA.
E-mail address: amoore@latech.edu (A.L. Moore).

https://doi.org/10.1016/j.addma.2021.102328
Received 4 May 2021; Received in revised form 23 August 2021; Accepted 13 September 2021
Available online 20 September 2021

excess of hot material occurs with an over extrusion event may lead to an abnormally high temperature or an irregular temperature trend in the vicinity of the event. For these reasons, there have been previous efforts to achieve real-time temperature monitoring of various types of AM processes [8,11]. The majority of these have involved a stationary, industry standard infrared (IR) thermal camera focused on a single print region to measure spatial and temporal temperature profiles of printed layers and corresponding sublayers during print. However, there are significant limitations when using a stationary temperature monitoring approach such as this. First, a stationary imaging system must be positioned to be able to view the full printing region of interest (ROI), which can negatively affect the resolution of fine features for larger ROI. Besides compromised spatial resolution, the ROI can easily be partially or entirely obscured by the moving extruder head assembly which increases the chance of missing crucial temperature profiles generated right after the extrusion of material. Due to the size of camera and its large field of view (FOV), it is often a challenge to set up the camera in an appropriate location of the 3D printer to get the desired view without any obstacle. Further, if real-time monitoring of temperatures is the end-goal of such measurements, there must be an associated back-end image analysis solution in place to translate the thermal images into actionable data. Depending on the size, complexity, and number of images to be analyzed, this may not be a trivial task.

An improved approach would instead use IR thermal sensors that move with the print head to monitor the ROI from a shorter working distance and with a FOV that includes on the recently extruded material and its immediate vicinity. In addition, the focus on the melt pool region by one or more sensors would facilitate more direct back-end analysis of their associated signal outputs as opposed to requiring image analyses. In one previous work that adopted this approach, a single IR temperature sensor was attached to an FDM printer to monitor the melt pool temperature along with a variety of other physical sensors in order to analyze signal patterns under different process conditions and to learn how they might correlate with process states and the evolution of build failure [12]. With respect to temperature sensing specifically, the use of a single sensor limits the ability of temperature monitoring to one specific direction. As the FDM printer extruder moves along both X and Y axes during printing, there will be a loss of usable temperature information for any of the two axes depending on extruder movements. This then suggests that a multi-sensor approach may be advantageous, but to the best of our knowledge has never been previously explored. This question of whether multiple sensors provide superior defect detection compared to single-sensor approaches forms the hypothesis investigated here.

In this work, a multi-sensor approach has been developed in which two IR thermal sensors are integrated within an FDM-based 3D printer such that there is a very short distance between the sensors and the extruder. In this way, a small target sensing area has been established near the melt pool region, i.e., the critical contact point where newly extruded material is deposited onto the workpiece surface. This enhances the sensors spatial sensitivity to defects. As the sensors move along with the extruder unit, they provide continuous in situ process monitoring and anomaly detection in real-time. Further, the use of multiple sensors allows for the temperature of the extruded material to be monitored regardless of X-Y translation direction. When this multi-sensor data is interpreted in conjunction with the G-code controlling the printer head, additional insight into local temperature distributions and defect location within the part can be obtained as compared to a single sensor. This approach is demonstrated for both a simple part geometry as well as a more complex industry standard test article. Strengths and limitations of this approach are presented, and the potential for expansion via more advanced data analysis techniques such as machine learning are discussed.

2. Methodology

2.1. Fused Deposition Modeling (FDM)-based 3D Printer

In an FDM printing process, the material is heated within an extruder head and then selectively deposited through a nozzle that traces the part's cross-sectional geometry to produce 3D parts directly from a CAD model in a layer-by-layer manner. A wide range of materials are available for this manufacturing process such as polylactic acid (PLA), acrylonitrile butadiene styrene, polycarbonate, and PCABS blend [13]. For the purpose of this work, a commercial FDM-based desktop 3D printer (LulzBot TAZ 6) was used as the example test. PLA was chosen as the printing material due to its widespread usage, though the calibration and sensing methods employed for this work can be easily applied to many other commonly used FDM materials. For printing of the PLA, the extruder temperature was set in the range of 205–210 °C and the print bed temperature was set to 60 °C. Printed samples were first drawn using commercial CAD software, and later the commercial slicing software CURA was used to convert the CAD STL file to a G-code file which ultimately controlled the motion of the printer head during a print process.

2.2. Selection of IR temperature sensor

A commercial IR temperature sensor (Texense IRN-2) was selected for this work based on its performance specifications and ease of integration. For the chosen 3D printer, the maximum extruder temperature reaches 210 °C during print. Thus, the specific Texense IRN-2 sensor model with a maximum temperature of 300 °C was selected to ensure that the sensing scale was optimized for achieving a strong and easily measured voltage signal output. The sensor accuracy is 2% of full scale while the output signal is on a 0–5 V scale per manufacturer specifications. As stated previously, it is advantageous for the FOV to be comparable to or slightly larger than the melt pool and its immediate vicinity. To achieve this, a custom aperture made of low emissivity highly polished aluminum with a center hole of 2.5 mm diameter was installed on the face of each sensor to reduce its standard FOV and tune its spatial resolution to that desired in this application. In its stock form, the sensors would have a spot size of approximately 8 mm diameter at the targeted working distance of 25 mm. With the custom apertures attached, the spot size of the sensors was found to be approximately 4 mm at the same working distance, which for an extruder nozzle diameter of 0.5 mm represents a sensing region roughly eight nozzle diameters across and was found to produce good results as shown via the results to be discussed in the following sections.

2.3. Calibration of IR sensor

When it comes to infrared temperature measurements, the apparent temperature of an object is a function of both its temperature and its thermal emissivity, which is a material property. For some surfaces, the emission of thermal radiation may also be dependent on the direction of observation. As a result, accuracy in temperature measurement requires calibration of IR sensors to the specific material, surface condition, and observation angle that will be utilized in practice. With this goal in mind, IR sensor calibration procedures were conducted for each individual sensor as shown in Fig. 1. The sample used for calibration was a 25 mm × 25 mm × 3.5 mm PLA part printed on the LulzBot Taz6 printer using the same printer settings as used for the printed parts analyzed later in this work. Beneath the PLA sample was a 25 mm × 25 mm thin film Kapton heater and two sets of thin 25 mm × 25 mm copper (Cu) plates. The two Cu plates were used to ensure better thermal contact and more uniform temperature distribution on the backside of the PLA sample. The Cu-heater-Cu sandwich was attached with the PLA sample using a thermally conductive epoxy. For temperature measurements, three J-type thermocouples were inserted inside the PLA sample through three 1 mm diameter holes which each extended to near the center line

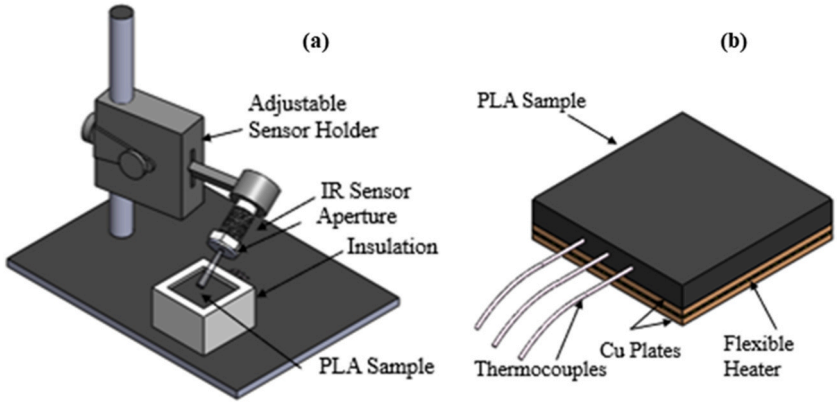

Fig. 1. Annotated illustrations of the IR sensor calibration (a) setup and (b) PLA sample.

of the calibration sample. Three thermocouples with 4 mm spacing were used in order to quantify the degree of temperature uniformity in the center of the sample where the IR sensor's viewing region would occur. Through all initial test runs, temperature differences of less than 1 °C were found between the three thermocouples which verifies that this setup succeeded in creating a uniform temperature distribution throughout the central region of the PLA sample to be used for IR sensor calibration.

Calibration was completed in two steps. In the first step, the temperature of the sample's top surface was measured via a fourth J-type thermocouple in direct contact with center of the top surface of the PLA sample. This was done to establish a known relationship between the temperatures measured by the three embedded thermocouples and the actual temperature at the top surface of the PLA sample. In the second step, the fourth thermocouple was removed, and the sample top surface was instead observed using the IRN-2 sensor. The sensor was first outfitted with the FOV-reducing aperture described above and oriented at the same design angle and working distance to be utilized when integrated onto the moving printer head. In this way, a sensor-specific correlation between a given IR sensor's IR voltage output and the surface temperature of the PLA was obtained for the same emissivity, surface condition, FOV, and direction of view as during actual printing, with representative results shown in Fig. 2. To associate the actual temperature at the top surface of the PLA sample obtained from the fourth thermocouple along with the IR sensor's voltage output, the embedded thermocouples average temperature was considered as the baseline. During calibrations, the sample's maximum top surface temperature was limited to approximately 80 °C to prevent the sample from deforming. Thus, to achieve voltage and temperature relations for higher temperature conditions, regression analysis and extrapolation was applied. Prior to performing the final calibration experiments, a test for angle dependency was conducted by taking data at 90° and 58.6°, where the latter is the designated angle for the sensor's eventual integration with printer head. No significant differences between the two data sets were observed, which led to the conclusion that the angular dependence for the IR temperature measurement was weak for this specific material and surface condition combination. In wider practice, because emissivity and surface roughness are material/print parameters, strictly speaking a change in feedstock or material should necessitate a new calibration be performed for each sensor. However, many polymers have similar emissivity values and if the surface roughness of the print will be unchanged, this may not be entirely necessary every time.

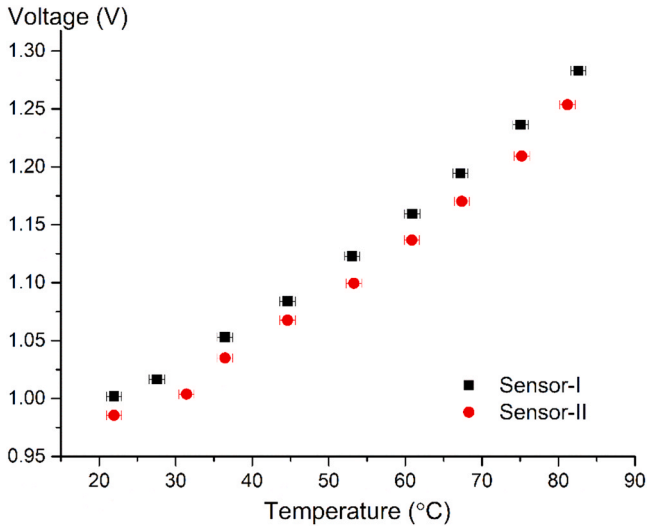

Fig. 2. Sensor signal output vs top surface temperature of PLA sample.

2.4. Sensor integration

Following calibration, the two IRN-2 sensors were attached to the 3D printer's extruder unit. Custom designed 3D printed brackets were used to hold the sensors at an angle of 58.6°, which is the angle at which the sensors can be mounted on the extruder unit to sense the appropriate printing zone without impeding any existing hardware (Fig. 3(a-b)). Both the sensor-bracket assemblies were mounted with the extruder unit such that one sensor's viewing spot follows the extruder from its front while the other sensor's viewing spot follows the extruder from its left side as shown conceptually in Fig. 3(c). In this way, the sensors provide temperature data for two different axes of movement of the extruder and facilitate the multi-directional observation capability of the in situ measurement system. During sensor integration, sensor-I was set at a working distance of 25 mm from its ROI (the region near melt pool in front of the extruder), and sensor-II was set at a working distance of 23 mm from its ROI (the melt pool region to the side of the extruder). As can be seen in Fig. 3, both sensors are located in close proximity to the extruder head hardware such that there is a possibility of signal contamination from the much hotter extruder impacting the IR signal being sought from the printed part. To mitigate this, a low emissivity polished aluminum sheet was installed around the extruder within the space between it and the sensors to act as a thermal radiation shield.

2.5. Design of print sample and intentional defect generation

For initial testing of in situ monitoring using the two IR sensors, a simple L-shaped sample was first utilized as shown in Fig. 4. According to the implemented sensor integration, sensor-I will be most effective during the + *Y*-axial movement of the extruder and sensor-II will be

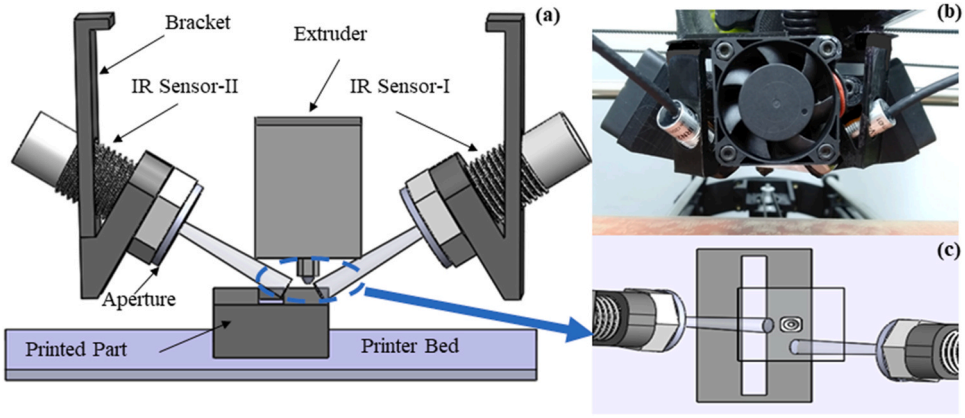

Fig. 3. (a) An illustration of sensors measuring melt pool temperature, (b) Image showing both sensors attached with the extruder head and (c) top view showing two different sensing zone for the sensors.

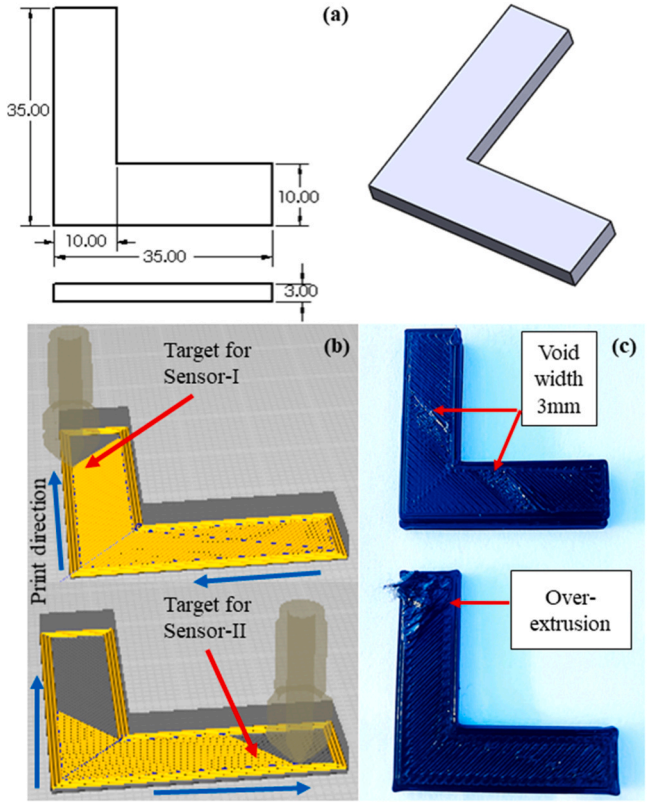

Fig. 4. (a) CAD images of the L-shaped sample (numbers in mm), (b) Layer view of printing taken from commercial slicing software and (c) Intentional defects on the L-shaped test print.

most effective during the $+X$-axial movement of the extruder.

The L-shaped sample designed here enables both the sensors to be ensured to be effective for more than two third of the duration of a single sample print. The STL file of the sample CAD was imported into the commercial slicing software CURA, which sliced the sample into 11 layers (8 skin layers and 3 fill layers). The layer view of the slicing software shows the print orientations for the different layers as given in Fig. 4(b). For layer-1, the extruder starts moving along the $-X$ direction and then turns at 90° to print along $+Y$ direction to complete the layer. Thus, for layer-1 only sensor-I remains effective as it senses the heated region near melt pool along the $+Y$ direction. For layer-2 the orientation changes. Now the extruder starts moving along $+X$ direction and after completing the horizontal part of the L-shaped sample's second layer, the extruder moves toward the vertical region of the sample and completes the layer by moving along $+Y$ direction again. Thus, for layer-2 both sensor-I and sensor-II will be effective for temperature sensing Fig. 4(b). The consecutive layers will be printed by alternating these two types of layer orientation.

After the design of the L-shaped test sample, a repeatable method of creating intentional defects at known locations within the sample was devised in order to quantify how well the sensors were able to detect defects or anomalies as they occurred. The two types of intentional defects able to be created and analyzed in this work are voids (lack of material) and over-extrusion (excess of material). The creation of intentional defects was achieved by manipulation of the G-Code that controls the print process after it was generated by the software but prior to initiating printing. By changing multiple extrusion commands within the G-Code, voids of controllable size at known locations were created during a given test print. To create an over-extrusion event, both feed rate and extrusion action commands within the G-Code were changed. Three different sizes of voids were implemented in which the void width was varied. The other two void size parameters i.e., length and height of voids, were constant and similar to sample width and layer height which are 10 mm and 0.25 mm, respectively. Fig. 4(c) shows representative examples of the two types of defects implemented via G-Code manipulation.

3. Analysis of temperature signals for defect detection

Test prints were done for standard profile, 40% infill, and without any build plate adhesion. As stated earlier, the L-shaped sample consisted of 11 layers (8 skin layers and 3 fill layers in a 4–3–4 combination). For every layer, printing started with the walls followed by the skins and fills. Fig. 5 shows a typical temperature signal versus time data set for a test run with no defects present, which we term a "good print" to distinguish from prints with defects. Regions in time corresponding to the printing of wall, skin, fill, and different layers are marked. This temperature versus time pattern for a good L-shaped part print was found to be highly repeatable between repeated runs.

To accomplish defect detection, a simple statistical approach was developed for this proof-of-concept study which is similar to a rudimentary form of machine learning. To create a reliable baseline data set for a good (defect-free) print against which to compare the defect-laden prints, temperature data obtained from three good prints was first averaged point-by-point in time. Then, the standard deviation σ of the three good prints were likewise determined point-by-point in time. By adding or subtracting a certain number of standard deviations from the averaged baseline data, an upper control limit (UCL = average + $n\ \sigma$) and lower control limit (LCL = average – $n\ \sigma$) control chart was created. By comparing the data from a test print against this control chart, the

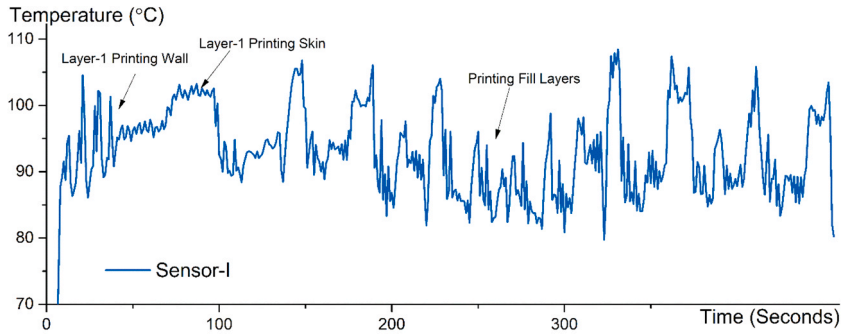

Fig. 5. A typical good print temperature plot of the L-shaped sample obtained from sensor-I.

presence of a given defect could be identified via violation of either the UCL or LCL at specific instances in time. After repeated calibration trials with defects of known location, it was determined that using $n = 3$ in the above definitions of UCL and LCL was able to reliably and repeatedly identify defect presence without creating frequent false positives where no defects were present.

In terms of sensor accuracy for defect detection, it is important to point out a few key aspects. First, as stated above the sensor accuracy is 2% of full scale per manufacturer specifications. This refers to the absolute temperature accuracy of the sensor, not its noise level. The actual output of the sensor is very stable for a given steady-state temperature, with noise on the order of <0.05% of the signal magnitude. Thus, the influence of random point-by-point error is minimal. Second, the independent calibrations performed for each sensor eliminates the influence of any sensor-to-sensor output variation. Third, the manner in which the sensors are utilized to identify defects is important. Because the detection scheme is based on comparison of the output from each sensor for a known "good print" against the output from those same sensors for a "test print" in question, any bias error not already accounted for via sensor-specific calibration would be present in both the "good print" data and the "test print" data taken with the same exact sensor. Thus, even if there is some residual absolute error present with a given sensor, via usage of a comparison approach the defect detection scheme employed here is still able to be effective.

3.1. Void defect detection

Intentional voids of different sizes were implemented in multiple locations and layers of the L-shaped sample, where over-extrusion was implemented only on the topmost layer of the sample into one known location. The defected samples were printed with a cold printer to get defect print temperature data from both of the sensors using a commercial data acquisition device. Fig. 6 shows temperature data taken during a test print with intentional void defects of varying sizes as well as one instance of an over-extrusion event. The UCL and LCL control chart data are also plotted for comparison and to evaluate defect

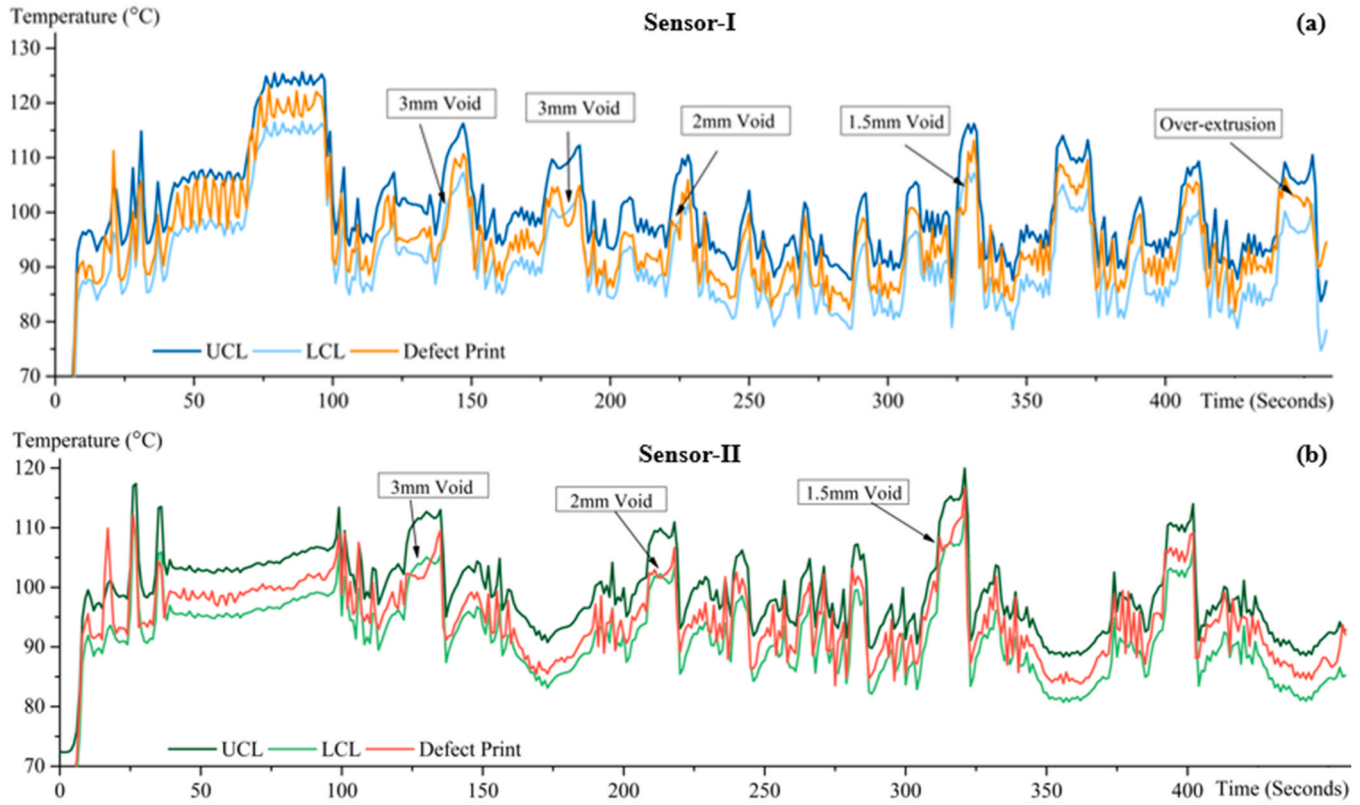

Fig. 6. $+/-3\sigma$ control chart comparing defected print temperature data with the control limits. (a) Control chart for sensor-I (b) Control chart for sensor-II comparing void and over-extrusion defects at multiple locations. Locations of defects introduced via G-code manipulation are indicated.

detection. As can be seen, the presence of a defect leads to a deviation of the temperature signal from the baseline as manifested by going below the LCL. Void defects as small as 1.5 mm of width were detected successfully at different layers of print by the +/- 3σ control chart. To evaluate the ability of increasing the sensitivity of the defect detection scheme, +/- 1.5 σ and +/- 2σ control charts were also tested for this case. However, this led to multiple instances of false positives where defects were flagged to have occurred when there were no defects present. Thus, the +/- 3σ control chart was chosen as being the most appropriate for this work. In order to illustrate this point visually, examples of UCL and LCL comparisons using a 1.5 σ, 2σ, and 3σ basis have been added into the Supplementary Material document as Figs. S1-S3, respectively.

Over repeated trials, voids implemented on different layers of the vertical part of L-shaped sample were always captured by sensor-I while moving at +Y direction. Three different sizes of voids were tested which are clearly visible by the sensor-I control chart's outliers as labeled in Fig. 6(a). Voids were also implemented in the horizontal part of the same L-shaped sample, but there were no significant fluctuations or valleys observed in the sensor-I control chart for those void defects. This result highlights the necessity of having more than one IR sensor in order to achieve robust defect detection along multiple head movement directions. For this example, the second sensor (sensor-II) captures IR signals at the +X direction and is thus able to detect these defects that sensor-I does not. Fig. 6(b) gives the sensor-II control chart for the same test print as shown for sensor-I in Fig. 6(a) and identifies the voids implemented on different layers of the L-shaped sample's horizontal part.

3.2. Over-extrusion defect and T-test for comparing slopes

Over-extrusion events were implemented only on the topmost layer (vertical part) of the L-shaped sample, with an example of an over-extrusion event's temperature signature marked in Fig. 6(a). Over-extrusion results in an excess of material being deposited in a specific region, with the exact directional movement of the excess material being unpredictable. If this excess molten material rolls or bulges into the FOV of a sensor, it can manifest itself as an unexpected positive change in slope within the temperature versus time data. If, however, the excess material causes a movement of material away from the targeted area/FOV, the defect manifests itself as an unexpected negative change in slope within the temperature versus time data. For the case shown in Fig. 6(a), instead of a drop in temperature outlying the LCL as seen for void defects, a significantly different slope is observed in the marked part of the control chart. This negative slope, while notably different from the baseline derived UCL and LCL lines, does not actually lead to a UCL or LCL violation. As a result, the simplistic UCL/LCL approach which was shown to be effective at identifying voids would not on its own be successful in flagging this as a print defect. Instead, the ability to detect an over-extrusion event requires the inclusion of a second statistical approach which determines the significance of the slope difference between baseline data and the test print at corresponding points in print time. A hypothesis test was conducted using a T-test for this purpose, where the null hypothesis is that there is no significant difference between baseline and test print slopes and the alternate hypothesis is that the difference between the slopes is significant. This T-test was conducted between the defective print data and the average of three good prints data, taking a moving average of sample size n = 5. P-values were obtained from the T-test calculations, which were then compared with a significance level (alpha) = 0.001. If the P-value chosen is lower than the decided significance level, then the null hypothesis is rejected and the alternate hypothesis is accepted. As an example, the lowest P-value was found to be 0.00082 at the over-extrusion event marked in Fig. 6(a), which is lower than the decided significance level. Thus, the deviation of slope method of identifying aberrations in printing behavior that do not necessarily violate UCL or LCL bounds is an effective means of detecting the occurrence of over-extrusion events or other defects that may not be found otherwise.

3.3. Standard test article results

After conducting these initial tests with the simplistic L-shaped sample, similar tests were performed on a different part geometry which was comparatively complex and covered more variations in extruder head movement. Thus, a new part geometry was chosen from literature which resembles the NAS 979 standard test article, also known as the circle diamond square test [12]. The version of the standard test article utilized in this work is shown in Fig. 7.

Creation of a baseline data set and its associated UCL and LCL was performed as before for the L-shaped part. Intentional voids were implemented on different features of the test article which are shown in Fig. 7(b). Defect print temperature data was then plotted in the control chart shown in Fig. 8 which is a break line plot of the original. Outliers from the LCL are visible for the voids implemented in the stepped regions and in the triangular features of the part. Outliers for these void defects were visible by sensor-I, while no outliers or significant fluctuations were found in the sensor-II data which again highlights the advantage of a multi-sensor approach. An over-extrusion defect was implemented at the end of the print and is also labeled in Fig. 8. Here, sensor-I data shows an increase of temperature which created an outlier to its UCL. Sensor-II, on the other hand, also showed a significant fluctuation but which was opposite to sensor-I and resulted in a LCL violation. This is hypothesized to be due to the unpredictable direction in which the over-extruded excess material flows as it builds up on the part surface, with more hot material being visible by one sensor and a lack of material being seen by the other in this instance. Regardless, the printing defect event was able to be seen as an aberration in the expected behavior by both sensors and thus flagged as an issue accordingly.

4. Discussion

Results presented in Figs. 6 and 8 show significant thermal fluctuations at the locations of intentionally implemented defects. However,

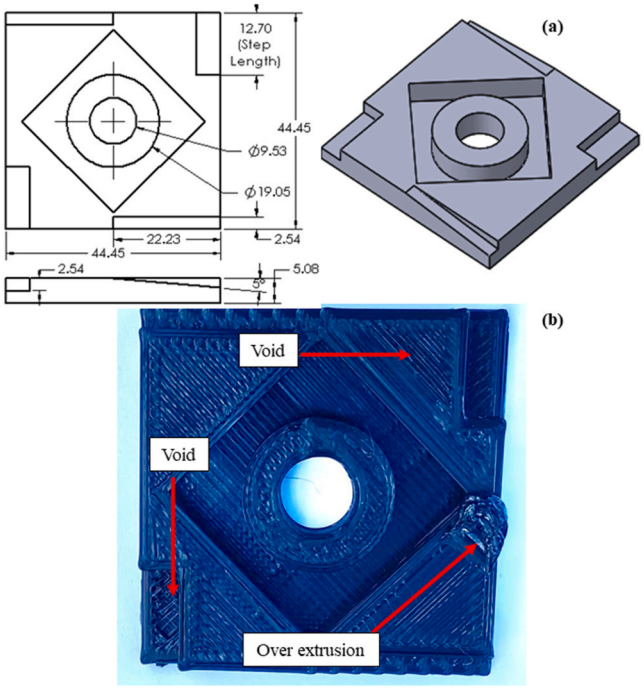

Fig. 7. (a) CAD images of the standard test article (dimensions in mm), (b) 3D printed standard test article with intentional defects.

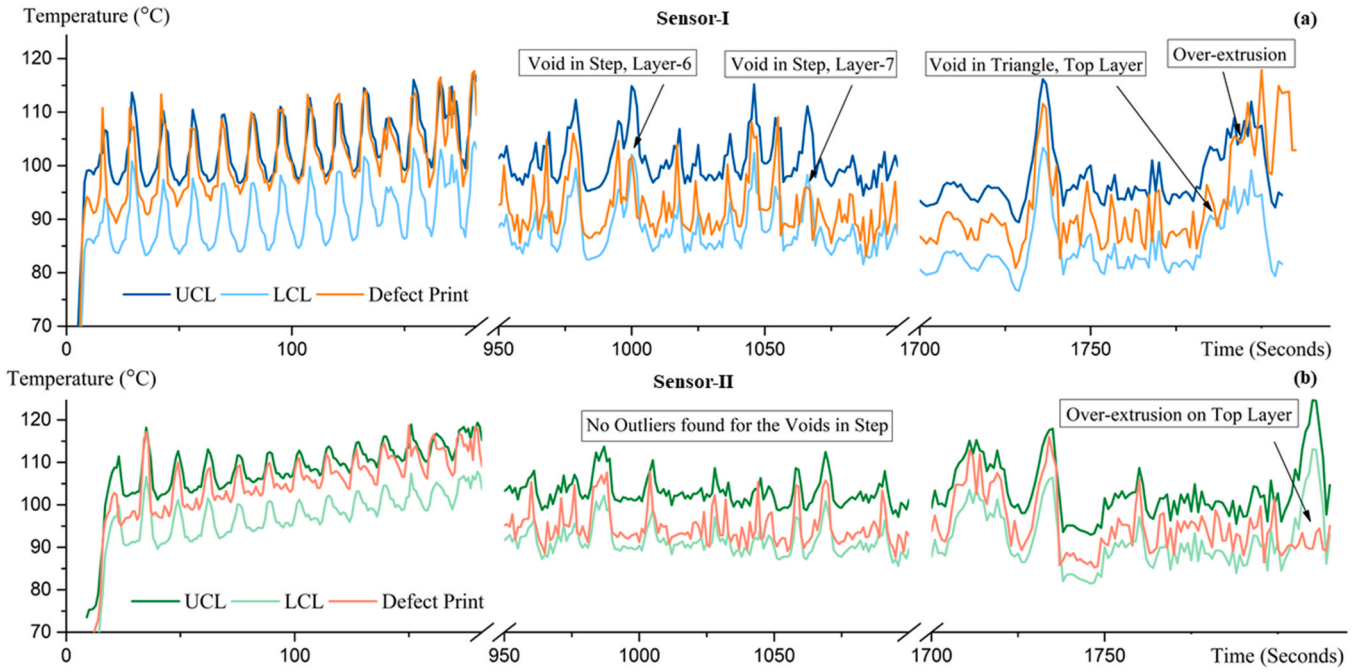

Fig. 8. (a) $+/-3\sigma$ control chart for sensor-I and (b) sensor-II comparing voids and over-extrusion defects at multiple locations within the standard test article. Break line plots are created due to the length of data.

not every defect was simultaneously observable by both sensors due to their differing orientations with respect to extruder head movement. This result supports the need for multiple sensors focusing on differing regions in order to achieve truly effective in situ defect detection in FDM-based AM. In this work, two sensors were implemented to sense at two different axial directions, with the integration of additional sensors being limited by the presence of existing hardware. However, we expect that two additional sensors may be required in order to ensure comprehensive monitoring.

The results presented here also demonstrate that the integrated IR sensors facilitate the detection of a minimum void width of around 1.5 mm. This resolution was achieved by using a customized aperture and by designing sensors working distance as small as possible without disturbing the printer's operation. Further decreasing the aperture size and working distance could lead to improved defect detection size resolution if the practical challenges of doing so can be overcome. Future works could investigate these changes to achieve a more robust monitoring approach for FDM-based AM. However, some changes would be specific to the printer model in question and may not necessarily translate to the broader field. Thus, in this work we focused on the broader topic of a general multi-sensor IR temperature-based approach towards in situ defect detection in real time.

In developing the means to interpret the raw temperature versus time data, two different statistical approaches were implemented in this work to detect and verify the significance of a temperature fluctuation. The simple statistical approaches for this proof-of-concept study were meant to mimic a rudimentary form of machine learning in which the algorithm receives baseline data as its training and compares incoming data to this learned behavior. First, a $+/-3\sigma$ control chart featuring baseline-associated UCL and LCL was applied to a given part geometry to locate features that violate the control limits. This worked well for void identification but did not always work for over-extrusion events. Next, a hypothesis test was able to test the significance of a slope deviation within the test data as compared to baseline data, which is helpful when only slope-like fluctuation is present instead of a UCL/LCL outlier. These experiences demonstrate that a robust data analysis scheme is an absolute requirement of an effective in situ monitoring solution, and that simple statistical methods such as these may not be infallible for complex printing patterns or specialized cases even if the temperature sensing aspects are working perfectly. Thus, a powerful and perhaps even necessary next step towards developing this technology would be to incorporate real machine learning into the process monitoring in which a more robust and complex algorithm with more inputs can be trained to recognize aberrations in the multi-sensor temperature data with greater reliability and precision than can be done by simple, traditional statistics as utilized here.

The eventual need for machine learning and automated data handling is even more apparent for more complex print geometries, longer print times, and more integrated sensors. The data generated from in situ monitoring under these conditions could be considerable. For example, in this work all preliminary analysis was done for an L-shaped test sample designed in a way that the sample was very basic but provided a print orientation that allowed both the sensors to be active for defect detection. Due to its simplicity, the number of print temperature patterns as well as their duration was very small; thus, defect detection with control charts was possible even with the naked eye. To experiment on a more complex and realistic geometry, a standard test article was then utilized. Several findings were observed during this test. For an over-extrusion defect two sensors at same time instance showed two different and opposite kind of fluctuations. Sensor-I showed outlier from the upper control limit and sensor-II showed outlier from the lower control limit. But for the simple L-shaped sample a negative slope was visible in the control chart. This led to a conclusion that, depending on print orientation, geometry of features, and defect position different types of fluctuations could be observed but may differ in their trend.

5. Conclusion

In this work, real time in situ detection of void and over-extrusion defects was effectively demonstrated using commercial components and fundamental statistical methods. The benefits of the multi-sensor approach were demonstrated, and the ability of the system to work with complex industry standard part geometries was shown. Voids as small as 1.5 mm width were successfully detected by both the sensors. Over-extrusion defects showed a significantly different slope instead of control limit violation, thus necessitating a multi-faceted approach to

statistical analysis of the temperature data. This multi-sensor approach along with the developed statistical data analysis has been shown here to be effective but could be significantly improved if combined with the algorithms of machine learning. With additional development, the multi-sensor temperature monitoring approach described here will not only provide an indication of defects like voids and over-extrusion, but also other anomalies such as filament breakage, clogged nozzle, or even unforeseen events which may lead to unsatisfactory part performance. In addition, this approach may help detect intentional sabotage attempts of printed parts by malicious parties through hacking of the AM hardware in order to induce defects.

CRediT authorship contribution statement

Rifat-E-Nur Hossain: Investigation, Writing – original draft. **Jerald Lewis:** Investigation, Writing – original draft, **Arden L. Moore:** Conceptualization, Writing – review & editing.

Declaration of Competing Interest

The authors declare that they have no known competing financial interests or personal relationships that could have appeared to influence the work reported in this paper.

Acknowledgements

This work was supported through the National Science Foundation and Louisiana Board of Regents via cooperative agreement OIA-1946231.

Appendix A. Supporting information

Supplementary data associated with this article can be found in the online version at doi:10.1016/j.addma.2021.102328.

References

[1] O. Holzmond, X. Li, In situ real time defect detection of 3D printed parts, Addit. Manuf. 17 (2017) 135–142, https://doi.org/10.1016/j.addma.2017.08.003.
[2] N. Montinaro, D. Cerniglia, G. Pitarresi, Defect detection in additively manufactured titanium prosthesis by flying laser scanning thermography, Procedia Struct. Integr. 12 (2018) 165–172, https://doi.org/10.1016/j.prostr.2018.11.098.
[3] M. Faes, W. Abbeloos, F. Vogeler, H. Valkenaers, K. Coppens, T. Goedemé, E. Ferraris, Process monitoring of extrusion based 3D printing via laser, Scanning (2016), https://doi.org/10.13140/2.1.5175.0081.
[4] D. Ye, G.S. Hong, Y. Zhang, K. Zhu, J.Y.H. Fuh, Defect detection in selective laser melting technology by acoustic signals with deep belief networks, Int. J. Adv. Manuf. Technol. 96 (2018) 2791–2801, https://doi.org/10.1007/s00170-018-1728-0.
[5] T.N.A.T. Rahim, A.M. Abdullah, H.Md Akil, Recent developments in fused deposition modeling-based 3D printing of polymers and their composites, Polym. Rev. 59 (2019) 589–624, https://doi.org/10.1080/15583724.2019.1597883.
[6] J. Straub, Initial work on the characterization of additive manufacturing (3D printing) using software image analysis, Machines 3 (2015) 55–71, https://doi.org/10.3390/machines3020055.
[7] J. Soete, B. Badoux, Y. Swolfs, L. Gorbatikh, M. Wevers, Defect detection in 3D printed carbon fibre composites using X-ray Computed Tomography, in: 9th Conf. Ind. Comput. Tomogr. Padova, Italy (ICT 2019), 2019, pp. 1–8. ⟨http://www.ndt.net/?id=23694⟩.
[8] J.E. Seppala, K.D. Migler, Infrared thermography of welding zones produced by polymer extrusion additive manufacturing, Addit. Manuf. 12 (2016) 71–76, https://doi.org/10.1016/j.addma.2016.06.007.
[9] M. Thompson, J.R. White, The effect of a temperature gradient on residual stresses and distortion in injection moldings, Polym. Eng. Sci. 24 (1984) 227–241, https://doi.org/10.1002/pen.760240402.
[10] V.E. Kuznetsov, A.N. Solonin, A. Tavitov, O. Urzhumtsev, A. Vakulik, Increasing strength of FFF three-dimensional printed parts by influencing on temperature-related parameters of the process, Rapid Prototyp. J. 26 (2020) 107–121, https://doi.org/10.1108/RPJ-01-2019-0017.
[11] L.M. Serio, D. Palumbo, U. Galietti, L.A.C. De Filippis, A.D. Ludovico, Monitoring of the friction stir welding process by means of thermography, Nondestruct. Test. Eval. 31 (2016) 371–383, https://doi.org/10.1080/10589759.2015.1121266.
[12] P.K. Rao, J. Liu, D. Roberson, Z. Kong, C. Williams, Online real-time quality monitoring in additive manufacturing processes using heterogeneous sensors, J. Manuf. Sci. Eng. Trans. ASME 137 (2015) 1–12, https://doi.org/10.1115/1.4029823.
[13] O.A. Mohamed, S.H. Masood, J.L. Bhowmik, Optimization of fused deposition modeling process parameters: a review of current research and future prospects, Adv. Manuf. 3 (2015) 42–53, https://doi.org/10.1007/s40436-014-0097-7.